China Geology 8 (2025) 475−486

China Geology

Journal homepage: http://chinageology.cgs.cn
https://www.sciencedirect.com/journal/china-geology

Mineral component of mineralizations in different types of breast lesions and their correlation with diseases

Chang-qiu Wang[a, b], Xiao Cheng[a], Xiao Ge[a], Hong-rui Ding[a], Yan Li[a], An-huai Lu[a,*]

[a] *Key Laboratory of Orogenic Belts and Crustal Evolution, MOE, School of Earth and Space Sciences, Peking University, Beijing* 100871, *China*
[b] *Gem Appraisal Center of Peking University, Beijing Co., Ltd., Beijing* 100871, *China*

ARTICLE INFO

Article history:
Received 7 April 2025
Received in revised form 6 June 2025
Accepted 9 June 2025
Available online 11 July 2025

Keywords:
Breast lesions
Invasive carcinoma
Carcinoma in situ
Benign lesions
Mineralization
Calcium phosphates
Calcium oxalate
Sustainable Development Goals (SDG 3)
Environmental geological survey engineering

ABSTRACT

Pathological mineralizations in breast lesions are closely associated with disease progression and serves as a critical diagnostic indicator. However, systematic understanding remains lacking regarding the phase categories, distribution patterns, and proportional occurrences of mineral phases across different breast lesion types. The diagnostic implications of specific phases, such as calcium oxalate, for distinguishing benign and malignant lesions remain controversial. This study employed polarizing microscopy, environmental scanning electron microscopy (SEM) with energy dispersive spectroscopy (EDS), transmission electron microscopy (TEM), Fourier transform infrared spectroscopy (FTIR), and Raman spectroscopy to analyze the phase composition of 61 mineralized samples from three lesion types: Invasive carcinoma, carcinoma in situ and benign lesions. Results demonstrate that breast lesion mineralizations predominantly comprise calcium phosphates, including hydroxyapatite (HA), amorphous calcium phosphate (ACP), and whitlockite, occasionally accompanied by calcium oxalate (monohydrate or dihydrate). Distinct distribution patterns and proportional occurrences of minerals were observed among the three types of lesion mineralizations. HA, as the predominant phase, was ubiquitously present across all three lesion categories. ACP, a mineralization precursor phase, emerged during early mineralization stages across all lesion types. Notably, whitlockite exclusively occurred in benign lesions and carcinoma in situ, with higher prevalence in benign cases, suggesting a progressive decline in Mg^{2+} concentration within the lesion microenvironment as malignancy advances. Calcium oxalate coexisted with HA in mineralized regions across all lesion types, and its presence in invasive carcinoma specimens warrants heightened clinical attention.

1. Introduction

Breast lesions encompass various types, which can be pathologically categorized into benign and malignant entities. Malignant breast cancer has become the most prevalent cancer in terms of incidence and mortality among women worldwide (Siegel RL et al., 2016), posing a significant threat to female health. Breast lesions are frequently associated with the formation of abnormal mineralization (O'Grady S and Morgan MP, 2018). Most breast mineralizations remain clinically undetectable due to their microscopic dimensions and diffuse distribution. However, their strong X-ray absorption and attenuation properties enable visualization as bright spots on radiographic images (Fischmann A, 2008), allowing disease-related information contained in non-palpable micromineralizations to be utilized for breast disease diagnosis through medical imaging modalities like mammography. In challenging clinical cases where conventional diagnostic methods prove inadequate, imaging-detected tissue mineralizations often serve as the sole marker for malignant lesions (Obenauer S et al., 2005). Micromineralization have emerged as one of the most crucial early diagnostic indicators for breast cancer (Ling H et al., 2013; O'Grady S and Morgan MP, 2018), and are postulated to exacerbate cancer cell dissemination and tissue invasion (Choi S et al., 2015). Notably, this pathological effect appears to vary with compositional alterations in the mineralizations (Scott R et al., 2017). Consequently, the compositional

First author: *E-mail address*: cqwang@pku.edu.cn (Chang-qiu Wang).

* Corresponding author: *E-mail address*: ahlu@pku.edu.cn (An-huai Lu).

Literary editor: Li-qiong Jia
doi:10.31035/cg20250062
2096-5192/© 2025 China Geology Editorial Office.

characteristics of breast mineralizations are believed to encode critical information closely associated with disease progression and pathogenesis (Fandos-Morera A et al., 1988).

Early classification systems categorized micro-mineralizations isolated from breast lesions into two primary types (I and II) based on their chemical composition and association with benign/malignant pathology. Type I mineralization, composed of calcium oxalate, is relatively rare and predominantly observed in benign lesions, with limited occurrence in malignancies (Frouge C et al., 1996). Type II mineralization, representing the most prevalent mineral phase in human breast lesions, consists of calcium phosphates, primarily hydroxyapatite (HA) or carbonate hydroxyapatite (CHA), and are detected in both benign and malignant conditions (Frappart L et al., 1986).

While no direct correlation exists between mineralization types and lesion malignancy, calcium oxalate has been proposed as a potential indicator of benign pathologies or lobular carcinoma in situ (LCIS) (Busing C et al., 1981; Frappart L et al., 1986; Haka AS et al., 2002; Morgan MP et al., 2005). Consequently, the detection of calcium oxalate often precludes further biopsy procedures in clinical practice (Stone N and Matousek P, 2008; Ghita A et al., 2018). However, paradoxical detection of calcium oxalate crystals in ductal carcinoma in situ (DCIS) and invasive ductal carcinoma (IDC) cases by Winston JS et al. (1992), Martin HM et al. (1999), and Scimeca M et al. (2014) challenges its specificity as a benign/LCIS marker. Furthermore, advanced spectroscopic analyses conducted by Kerssens M (2012), particularly through infrared spectroscopy and synchrotron radiation X-ray diffraction (SRXRD), have identified additional mineral phases such as whitlockite within breast calcifications, revealing greater compositional complexity than previously recognized.

Breast mineralizations play a critical role in mammary disease diagnosis, with its heterogeneous characteristics demonstrating potential diagnostic value for lesion classification. However, systematic understanding of phase composition in pathological breast mineralizations remained incomplete. The controversy persists regarding the prognostic significance of mineralization variability in differentiating benign and malignant lesions. This study conducts an in-depth investigation into the phase diversity of breast mineralizations, specifically examining the prevalence and proportional distribution of distinct mineral phases across three pathological categories: Invasive carcinoma, carcinoma in situ, and benign lesions. The research aims to establish mineralogical evidence elucidating the relationship between mineralization phase composition and breast lesion types.

2. Materials and methods

A total of 61 breast tissue specimens with distinct mineralization were selected from the medical archives of Peking University Third Hospital, Beijing Hospital, and Hubei Zhongxiang People's Hospital, comprising three diagnostic categories that form a malignancy-gradient test series (invasive → in situ → benign). The lesion types included invasive carcinomas (invasive ductal carcinoma and invasive lobular carcinoma), carcinomas in situ (ductal carcinoma in situ and lobular carcinoma in situ), and benign lesions (fibroadenoma, usual ductal hyperplasia, ductal ectasia, and sclerosing adenosis). The cohort consisted of 25 invasive carcinoma cases (designated JR-1~25), 15 carcinoma in situ cases (YW-1~15), and 21 benign lesion cases (LX-1~21). Continuous sectioning of paraffin-embedded tissue blocks was performed using a Leica ultramicrotome. For each specimen, one 4-μm section was prepared as a standard hematoxylin-eosin (HE) stained slide, one 8-μm section mounted on a 20 mm × 20 mm silicon wafer, and one 8-μm section placed on a clean glass slide as a blank control. Multiple consecutive sections were stored in 1.5 mL centrifuge tubes for subsequent isolation of mineralization powder following established protocols detailed by Meng FL et al. (2015).

HE-stained slides were analyzed under a Nikon LV100 POL polarized light microscope (POM) at the Microscopy Laboratory of School of Earth and Space Sciences, Peking University to document mineralization size, morphology, and distribution patterns, while simultaneously enabling sample selection and preliminary localization for subsequent analyses. Chromium-coated silicon wafer samples were examined using a Quanta 650FEG field-emission environmental scanning electron microscope (ESEM) equipped with energy-dispersive X-ray spectroscopy (EDX) at the same institution, revealing mineralization distribution characteristics and elemental composition. Isolated mineralization samples underwent ultrasonic dispersion in anhydrous ethanol for 10 minutes to create homogeneous suspensions, which were deposited onto microgrids using disposable pipettes. After air-drying, these preparations were analyzed with a JEM-2100F field-emission high-resolution transmission electron microscope (TEM) at Analytical Testing Center of Peking University to acquire morphological and structural information, including lattice fringe images and electron diffraction patterns from selected areas. Fourier-transform infrared (FTIR) spectroscopy was performed using a NICOLET iN10 MX microspectrometer at the University's College of Chemistry and Molecular Engineering, where dried mineralization powders were compressed between diamond anvils and analyzed across the 650–4000 cm^{-1} spectral range. Resultant spectra were compared against reference mineral spectra in the Sadtler database for phase identification. Raman spectroscopic analysis was conducted using a Renishaw inVia Reflex confocal microspectrometer at the Beijing Key Laboratory of Mineral Environmental Function (School of Earth and Space Sciences, Peking University), with either adhered powder samples or blank control slides analyzed across 400–1300 cm^{-1} spectral range to characterize phase composition.

3. Results

3.1. Polarized Optical Microscopy (POM) observations

POM examination of hematoxylin-eosin (HE)-stained

sections from all 61 cases across three pathological types revealed variably abundant deeply stained mineralization (Fig. 1). The mineralization exhibited irregular flaky morphologies (outlined by red solid circles in Fig. 1) or subrounded shapes (yellow solid circles in Fig. 1), with substantial diameter variations. Distinct psammoma body-like concentric lamellar structures were observed in some regions (indicated by yellow arrows in Fig. 1). Both morphological types of mineralization occurred across all three lesion categories.

A characteristic extinction phenomenon with alternating light-dark variations under cross-polarized light was identified in selected sections, manifesting as four distinct extinction positions per full rotation, accompanied by white or yellowish-white flashes between extinction angles, indicative of calcium oxalate presence (Chen SG, 1993). This optical signature was detected in one invasive carcinoma, one carcinoma in situ, and three benign lesion cases.

In carcinoma in situ sample YW-2, calcium oxalate mineralization remained unstained by HE under plane-polarized light, displaying pale amber coloration (green arrow in Fig. 2a). Under cross-polarized light, these areas exhibited sharp white flashes with well-defined boundaries (yellow arrow in Fig. 2b), demonstrating four cyclical bright-dark transitions during stage rotation. In contrast, type II calcium phosphate mineralization displayed basophilic staining properties, appearing dark bluish-purple in HE-stained sections (Fig. 2c). No resolvable extinction variations were observed under cross-polarized rotation, exhibiting quasi-isotropic "complete extinction" behavior (Fig. 2d). The predominant HA composition in calcium phosphate mineralization likely accounts for this phenomenon, with contributing factors including nanocrystalline grain size (<1 μm), low birefringence (weak interference colors), and light absorption by histological stains.

3.2. Environmental Scanning Electron Microscopy (ESEM) analysis

ESEM observations revealed significant morphological diversity in breast lesion mineralization, primarily categorized into two distinct patterns: (1) Extensive sheet-like mineralization localized within ductal lumina (Fig. 3a) or associated with collagen fibers, and (2) spheroidal mineralization with variable diameters ranging from several micrometers to submicron scales, adherent to collagenous matrices (Fig. 3b).

Energy-dispersive X-ray (EDX) spot analysis of 61 in situ silicon-mounted samples across all three lesion types demonstrated broad Ca/P atomic ratio (At%) variations (1.212–2.394). Quantitative elemental mapping of sheet-like and spheroidal mineralization patterns (averaged from n=5 measurements per feature) identified calcium (Ca), phosphorus (P), carbon (C), and oxygen (O) as primary

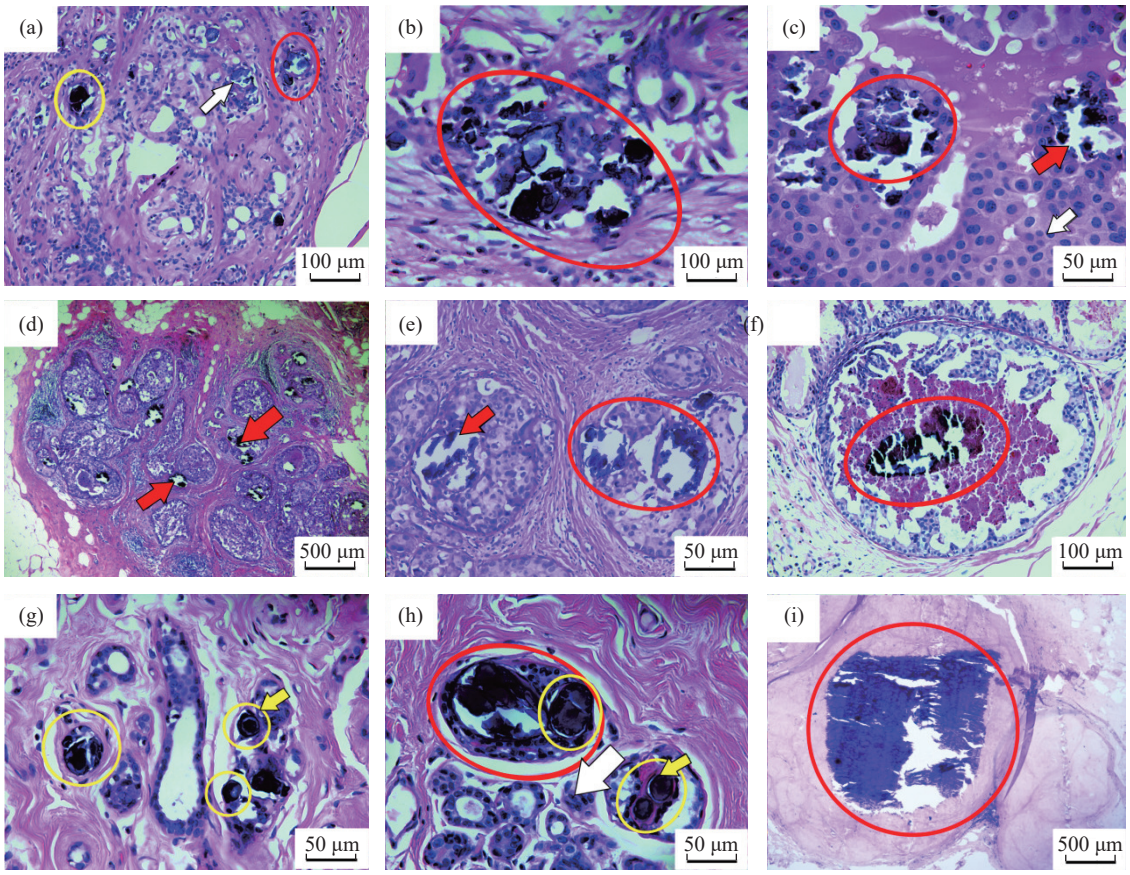

Fig. 1. HE-stained sections showing mineralization in various types of breast lesions. a–c–invasive carcinoma; d–f–carcinoma in situ; g–i–benign lesions.

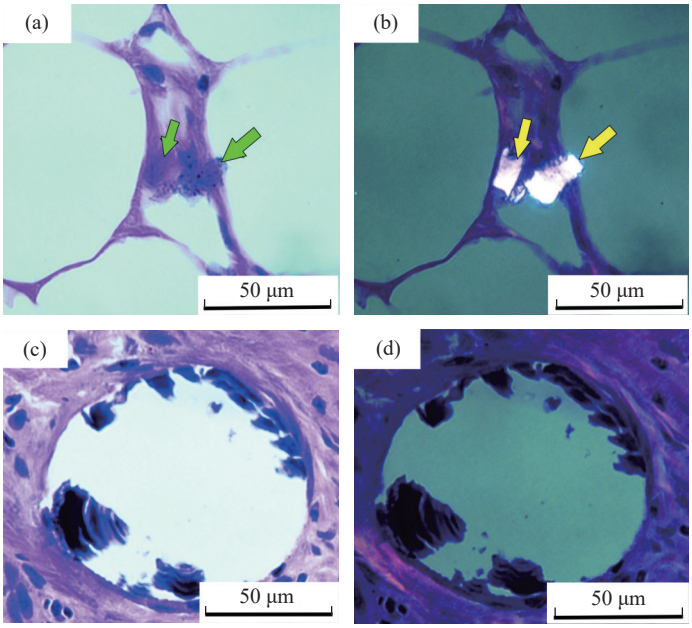

Fig. 2. Polarized light micrographs of type I and II mineralization in breast carcinoma in situ sample YW-2. a, b–histological images of type I calcium oxalate mineralization under plane-polarized and cross-polarized light, respectively. c, d–histological images of type II calcium phosphate mineralization under plane-polarized and cross-polarized light, respectively.

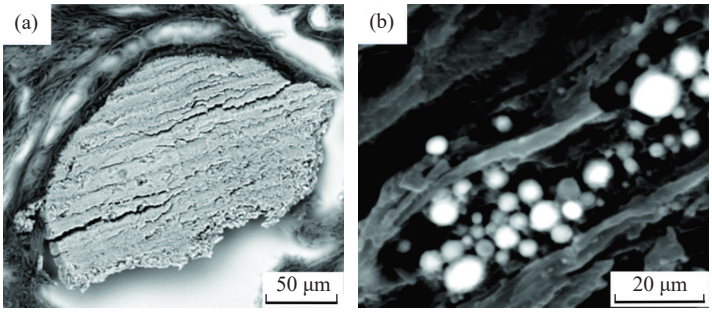

Fig. 3. ESEM backscattered electron images of breast lesion mineralization. a–sheet-like mineralization within a ductal lumen; b–collagen-associated spheroidal mineralization.

constituents, with a mean Ca/P ratio of 1.645 (Fig. 4). This value aligns with the theoretical Ca/P range for HA in human biomineralization systems (Dorozhkin SV, 2010).

ESEM imaging further identified amorphous mineralization regions characterized by loose flocculent textures containing irregular submicron spheroids and interstitial amorphous material (Fig. 5). EDX analysis of these regions (n=10 measurements) revealed a mean Ca/P ratio of 1.320 (Fig. 5), consistent with amorphous calcium phosphate (ACP) as defined by Mahamid J et al. (2008).

Polyhedral mineralization with well-defined crystallinity was observed across all lesion types (Fig. 6). Comparative analysis demonstrated subtle morphological variations among invasive carcinoma (JR-8, Fig. 6a), carcinoma in situ (YW-7, Fig. 6b), and benign lesion (LX-4, Fig. 6c) specimens, with partial fragmentation noted in invasive carcinoma-associated mineralization. EDX spot analysis (n=2–5 measurements per structure) of these polyhedral features detected calcium, carbon, and oxygen as exclusive constituents (Table 1). The atomic ratio of Ca: C approximated 1∶2 across all three lesion types, corresponding to the stoichiometric composition of calcium oxalate ($Ca[C_2O_4]$), suggesting potential calcium oxalate mineralization coexistence in diverse breast pathologies.

3.3. Transmission Electron Microscopy (TEM) analysis

The crystalline morphology of mineralization in three types of breast lesions after isolation was observed under TEM, revealing diverse microcrystalline configurations and their aggregates, including rod/particulate (Figs. 7a, d, g), fibrous (Figs. 7b, e, h), columnar (Fig. 7f), and spheroidal forms (indicated by red circles in Figs. 7b, c, i). These mineralization morphologies were identified across all three types of breast lesion samples, with coexistence of different crystal forms observed in specific instances (Figs. 7b, c). The rod/particulate crystals exhibited relatively regular geometry, with further magnification demonstrating overlapping and stacking of particles, displaying short-edge dimensions below 10 nm and long-edge dimensions reaching 50 nm. In contrast, fibrous crystals demonstrated irregular morphology and comparatively poorer overall crystallinity. The spheroidal structures in Fig. 7i presented as uniformly rounded entities

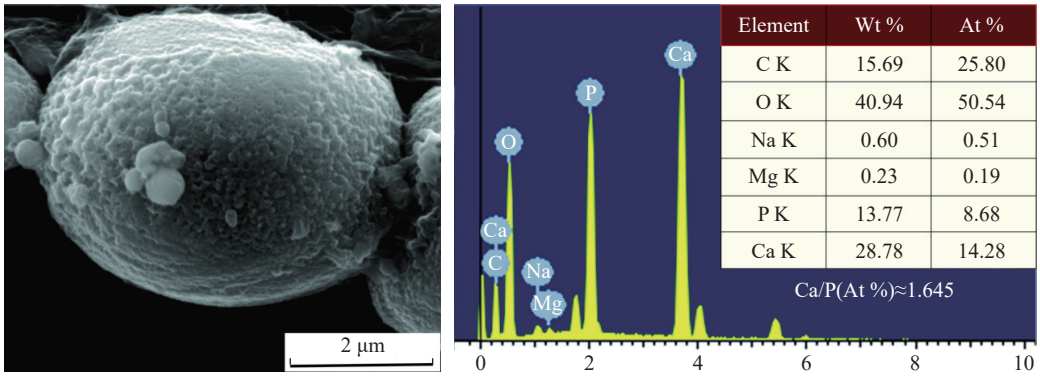

Fig. 4. ESEM micrographs and EDX profiles of breast lesion mineralization.

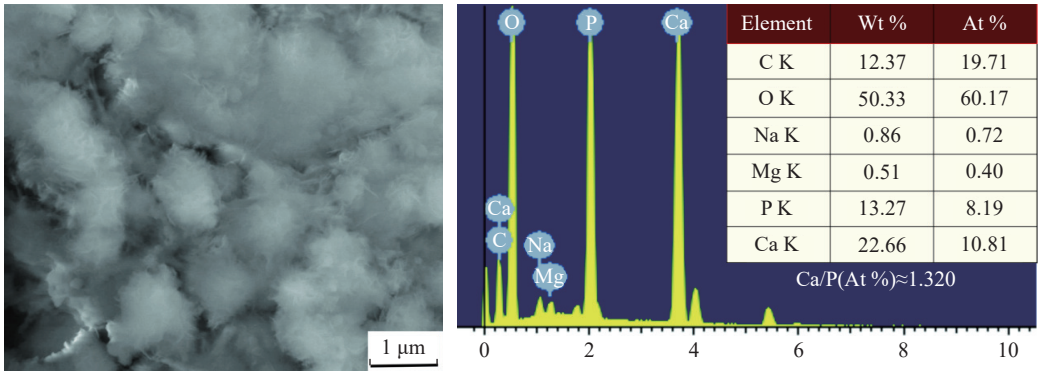

Fig. 5. ESEM morphology and EDX analysis of amorphous mineralization regions.

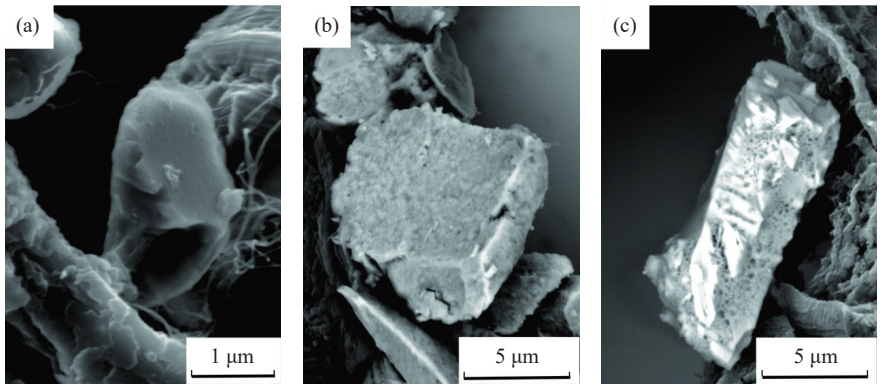

Fig. 6. Polyhedral mineralization in breast lesions. a–invasive carcinoma JR-8; b–carcinoma in situ YW-7; c–benign lesion LX-4.

Table 1. EDX results of three morphologically distinct mineralization specimens.

	Element	C	O	Mg	Ca	Total
a (JR-8)	wt%	15.77	54.63	–	29.60	100.00
	At%	24.02	62.47	–	13.51	
b (YW-7)	wt%	16.44	54.09	0.26	29.21	
	At%	24.93	61.60	0.19	13.28	
c (LX-4)	wt%	15.25	49.99	–	34.76	
	At%	24.48	61.84	–	13.68	

with high crystallinity and dense architecture, exhibiting electron beam impermeability. Conversely, spheroidal structures in Figs. 7b and 7c displayed looser organization, with detailed observation revealing their composite nature formed by aggregated smaller particulate crystals.

Lattice fringe imaging and selected-area electron diffraction (SAED) were performed on ultrathin specimen edges using Digital Micrograph software for interplanar spacing measurement and pattern indexing. Calibration against standard PDF cards (Frondel C, 1943) identified d-spacings of 2.81 Å, 3.51 Å, 2.27 Å, 2.53 Å, 2.14 Å, and 2.73 Å, corresponding to HA lattice planes (2 1 1), (2 0 1), (3 1 0), (3 0 1), (3 1 1), and (3 0 0), respectively (Figs. 8a, c, e). The electron diffraction patterns of mineralization exhibited polycrystalline ring configurations (Figs. 8b, d, f), indicating that the samples consisted of nanocrystalline polycrystals. A limited number of diffraction rings were observed, with inner rings demonstrating relatively sharp definition while outer

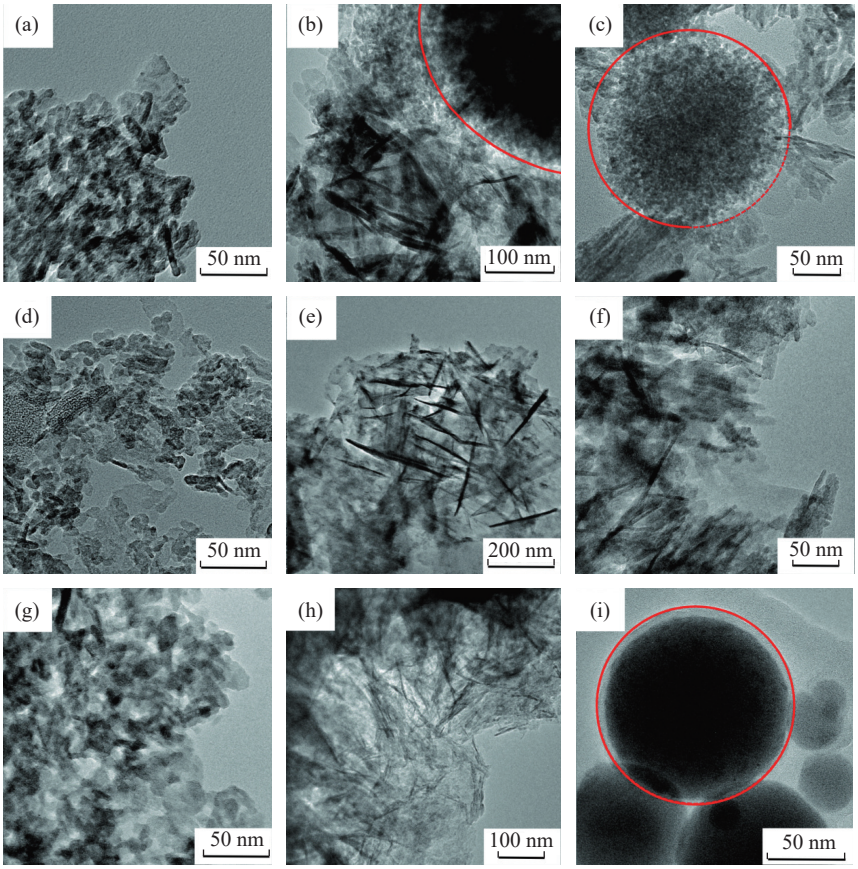

Fig. 7. TEM morphologies of breast lesion mineralization. a–c–invasive carcinoma; d–f–carcinoma in situ; g–i–benign lesions.

rings exhibited diffuse dispersion, collectively suggesting low crystallinity of the mineralization. Indexing results of all diffraction rings matched the reference parameters of HA (Frondel C, 1943), confirming its ubiquitous presence in mineralization from invasive carcinoma, carcinoma in situ, and benign lesion specimens.

Non-HA phases were detected in some samples (Fig. 9). Under TEM imaging, well-crystallized rounded spheroidal mineralization with a diameter of approximately 350 nm was observed in the benign breast lesion sample LX-4 (Fig. 9a). Its selected-area electron diffraction (SAED) pattern (selected area size about 200 nm×200 nm) exhibited periodically and symmetrically arranged diffraction spots (Fig. 9b), corresponding to the characteristic diffraction pattern of a single crystal.

The diffraction pattern in Fig. 9b was calibrated using Digital Micrograph software to generate Fig. 10. By measuring the smallest fundamental unit (characteristic parallelogram) within the pattern, the distances R_1≈1.935 nm, R_2≈1.240 nm, and R_3≈5.998 nm were obtained. Using the diffraction formula $R=L\lambda/d$, the corresponding interplanar spacings were calculated as 5.17 Å, 8.06 Å, and 3.33 Å, respectively. These values align with the parameters from the whitlockite PDF card (Hanawalt J et al., 1938), with the three diffraction spots corresponding to the (1 1 0), (0 1 2), and (1 2 2) crystallographic planes of whitlockite (Hanawalt J et al., 1938), confirming its composition as the primary mineralization phase.

Smaller-diameter spheroids likely represent early-stage mineralization, as shown by densely packed mineralization spheroids (diameter <50 nm) with homogeneous internal structures in Fig. 11a. Imaging of thinner edge regions revealed indistinct lattice fringes (white solid-line box in Fig. 11b), while the central white box showed no discernible lattice features. The SAED pattern from the yellow dashed-line box in Fig. 11b displayed coexisting diffraction spots and diffuse rings (Fig. 11c). The diffraction spots, indexed to the (0 0 2), (2 1 0), and (1 1 2) planes of HA (PDF2-2004; 00-090-0432), indicate localized crystalline regions with sparse crystal distribution. The diffuse rings, characteristic of amorphous calcium phosphate, confirm the coexistence of amorphous and crystalline phases in this region.

3.4. Fourier Transform Infrared Spectroscopy (FTIR) analysis

The transmission-mode micro-FTIR testing of mineralized powders from three types of separated breast tissue samples revealed characteristic infrared spectra of HA in all samples (Fig. 12). The strongest peak near 1036 cm^{-1} corresponds to the antisymmetric stretching vibration $\nu_3(PO_4^{3-})$ of phosphate groups, while the minor peak near 960 cm^{-1} represents the symmetric stretching vibration $\nu_1(PO_4^{3-})$ of phosphate groups. The peak near 3435 cm^{-1} is attributed to the stretching vibration $\nu(OH^-)$ of hydroxyl groups. These peaks collectively serve as characteristic signatures of HA (Rey C et

al., 1989), indicating the presence of HA in the mineralization from invasive breast carcinoma, ductal carcinoma in situ, and benign lesions. Additionally, the infrared spectra exhibit the characteristic peak of Amide I near 1626 cm^{-1}, suggesting a close association between mineralization and organic components. The spectra also display the out-of-plane bending vibration $\nu_2(CO_3^{2-})$ of carbonate groups near 873 cm^{-1} and the antisymmetric stretching vibration $\nu_3(CO_3^{2-})$ as a doublet near 1419 cm^{-1} and 1454 cm^{-1}, indicating partial carbonate substitution in mineralized HA.

Infrared spectra of individual samples revealed characteristic peaks of calcium oxalate (Fig. 13). In addition to HA signatures, the vibrational peaks at 781 cm^{-1} and 665 cm^{-1} were identified as key diagnostic features of calcium oxalate monohydrate. A bending vibration peak of coordinated water in calcium oxalate was observed near 1640 cm^{-1}, intermediate between the 1620 cm^{-1} peak of calcium oxalate monohydrate and the 1646 cm^{-1} peak of calcium oxalate dihydrate. A medium-intensity peak at 1321 cm^{-1} corresponds to the metal-carboxyl stretching vibration, positioned between the 1316 cm^{-1} peak of calcium oxalate monohydrate and the 1324 cm^{-1} peak of calcium oxalate dihydrate. A broad, non-split peak near 3430 cm^{-1} typically represents the symmetric and antisymmetric stretching vibrations of coordinated water in calcium oxalate. Notably, the prominent water-related peak of OH^- between 3300–3400 cm^{-1} often overlaps with vibration peaks from coordinated water in calcium oxalate. The presence of these spectral bands confirms the existence of calcium oxalate crystals in this specific mineralization case.

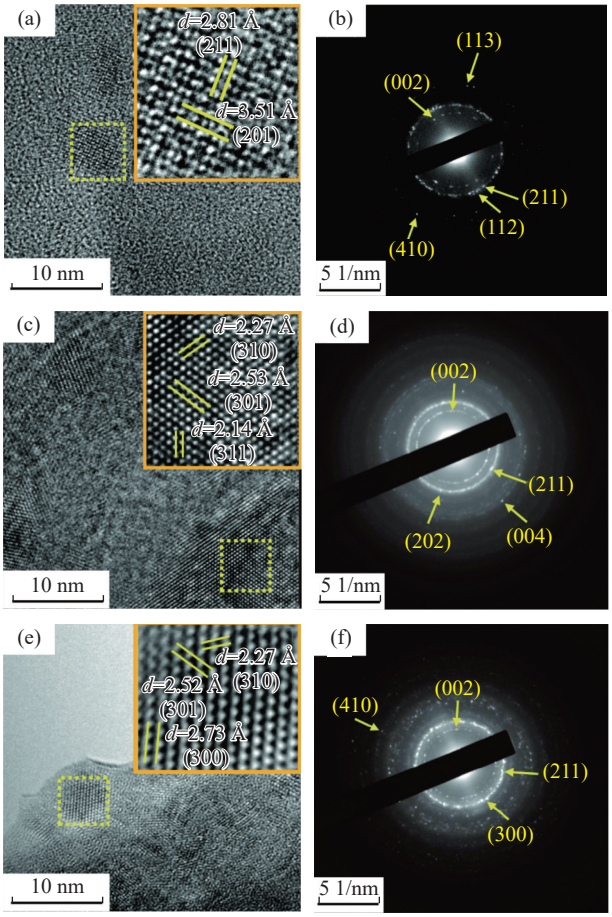

Fig. 8. Lattice images and electron diffraction patterns of mineralization. a–b–invasive carcinoma; c–d–carcinoma in situ; e–f–benign lesions.

3.5. Micro-Raman spectroscopy analysis

Micro-Raman spectroscopy analysis revealed that all samples exhibited characteristic Raman spectra of HA (Fig. 14). The single peak near 960 cm^{-1} corresponds to the symmetric stretching vibration $\nu_1(PO_4^{3-})$ of phosphate groups, representing the characteristic peak of HA (You AF et al., 2017). The Raman peaks at 434 cm^{-1} and 593 cm^{-1} are attributed to the in-plane bending vibration $\nu_2(PO_4^{3-})$ and out-of-plane bending vibration $\nu_4(PO_4^{3-})$ of phosphate groups in HA, respectively. The peak at 1070 cm^{-1} arises from the asymmetric stretching vibration $\nu_3(PO_4^{3-})$ of phosphate groups and the $\nu_1(CO_3^{2-})$ mode of carbonate groups, serving as a characteristic peak for type B carbonate substitution (CO_3^{2-} substituting PO_4^{3-}). Additionally, a weak peak near 1001 cm^{-1} was observed in the benign lesion sample LX-1, which may originate from C-C vibrations of organic components (Xu CQ et al., 2009).

Characteristic peaks of whitlockite were detected in some powdered samples (Fig. 15). Under 50× objective lens, the mineralization powder from ductal carcinoma in situ sample YW-7 exhibited rounded microspheres (diameter <5 μm) at location “a”, with the strongest Raman peak at 968 cm^{-1}.

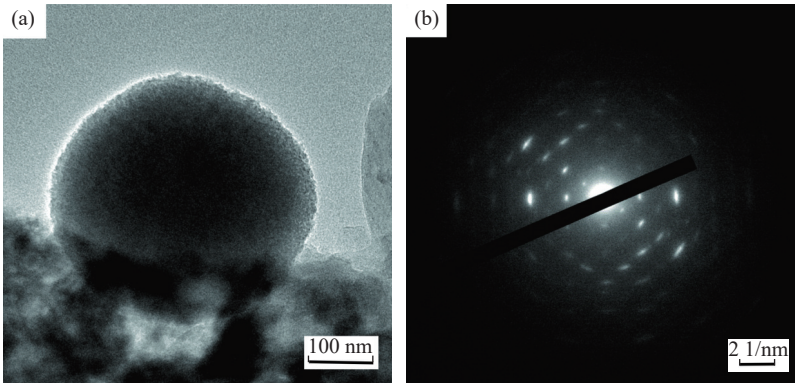

Fig. 9. TEM morphology (a) and diffraction pattern (b) of benign lesion LX-4.

No.	*h*	*k*	*l*	*d*/Å	2*θ*/Å	*I*/%
1	0	1	2	8.06996	10.955	11.5
2	1	0	4	6.44415	13.731	16.7
3	0	0	6	6.18083	14.318	0.9
4	1	1	0	5.17500	17.121	55.4
5	1	1	3	4.77358	18.573	1.0
6	2	0	2	4.35625	20.370	5.1
7	0	1	8	4.11756	21.564	1.9
8	0	2	4	4.03498	22.011	16.0
9	1	1	6	3.96786	22.388	2.9
10	1	0	10	3.42678	25.981	40.6
11	2	1	1	3.37378	26.396	4.4
12	1	2	2	3.33266	26.728	10.3
13	1	1	9	3.22351	27.651	5.2

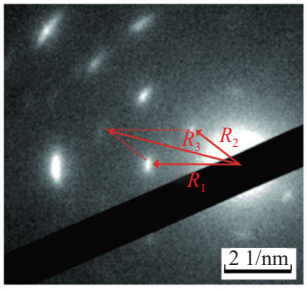

R_i/nm	d_i/Å	*hkl*
1.935	5.17	(110)
1.240	8.06	(012)
5.998	3.33	(122)

Fig. 10. Indexing results of diffraction pattern.

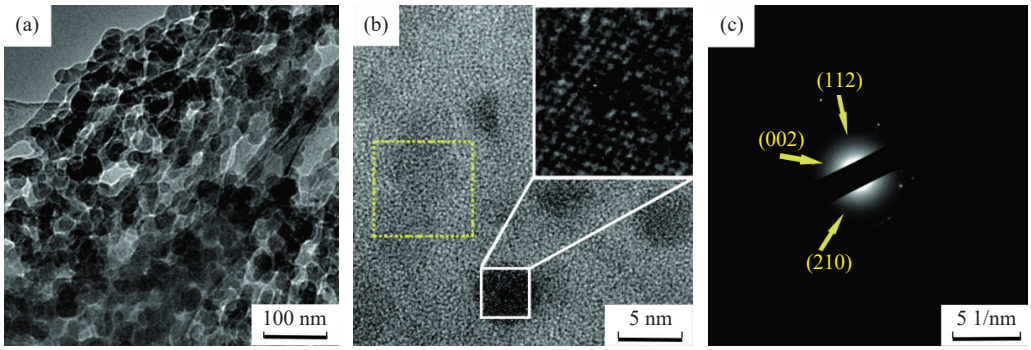

Fig. 11. Sub-50 nm mineralization spheres. a–overview morphology; b–high-resolution image; c–diffraction pattern from yellow-dashed region.

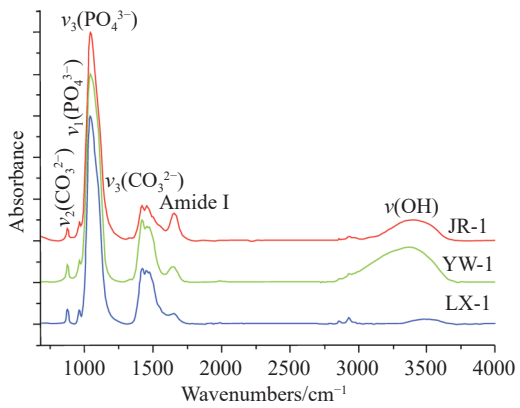

Fig. 12. Infrared spectra of three types of breast lesions: samples JR-1, YW-1, and LX-1 (1#).

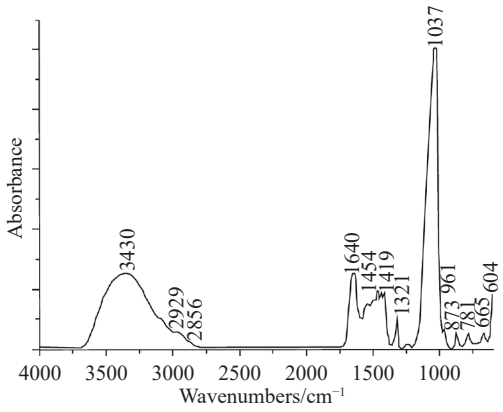

Fig. 13. Infrared spectrum of ductal carcinoma in situ sample YW-2 (2#).

Location “b” showed a mixed area of microspheres and irregular blocks, displaying the strongest Raman peak at 965 cm^{-1}. Location “c” consisted of densely structured irregular blocks, with the strongest Raman peak at 961 cm^{-1}. The 960 cm^{-1} Raman shift is recognized as a characteristic peak of HA (You AF et al., 2017), while the phosphate stretching vibration peak near 970 cm^{-1} indicates the presence of whitlockite (Xu CQ et al., 2009; You AF et al., 2017). These observations suggest that location “a” primarily contains whitlockite, location “c” contains HA, and location “b” represents a mixture of HA and whitlockite. Samples exhibiting whitlockite characteristic peaks included 2 cases of carcinoma in situ and 5 cases of benign lesions, with no such peaks detected in invasive carcinoma samples.

Micro-Raman analysis was performed on unstained slides showing quadruple bright-dark extinction phenomena under polarized microscopy to further verify the presence of calcium oxalate. Taking invasive breast carcinoma sample JR-8 as an example (Figs. 16a, b), Raman testing of the arrow-indicated region yielded a spectrum (Fig. 16c) with the strongest peak at

912 cm^{-1}, accompanied by a medium-intensity peak at 505 cm^{-1} and a weak peak at 873 cm^{-1}. These features are consistent with previously reported Raman spectra of calcium oxalate dihydrate (Haka AS et al., 2002; Saha A et al., 2011; Wang ZT et al., 2014). Comprehensive micro-Raman analysis demonstrated: Among 25 invasive carcinoma samples, 1 case showed coexisting type I/II mineralization while the remaining 24 exhibited only type II mineralization; among 15 carcinoma in situ samples, 1 case showed coexisting type I/II mineralization while others displayed pure type II mineralization; Of 21 benign lesions, 3 cases presented mixed type I/II mineralization with the remaining 18 showing type II mineralization exclusively.

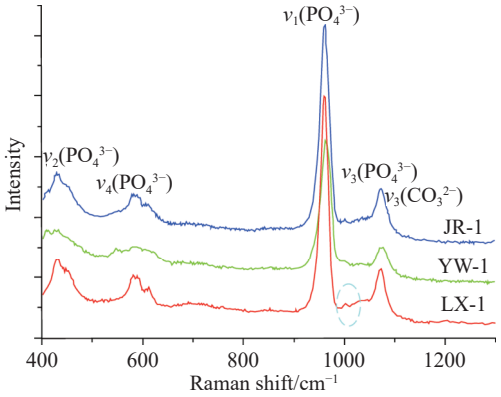

Fig. 14. Raman spectra of three types of breast lesion samples (1# JR-1, YW-1, and LX-1).

4. Discussion

As the most stable calcium phosphate mineral in physiological pH environments, HA has long been recognized as the primary phase composition in mammary lesion mineralization (Frappart L et al., 1986; Haka AS et al., 2002; Wang CQ et al., 2011; Meng FL et al., 2015). Systematic testing of mineral phases in mammary tissue mineralization from three distinct pathological types - invasive carcinoma, carcinoma in situ, and benign lesions - conducted in this study reveals that, in addition to HA, mammary lesion mineralization also contains ACP, calcium oxalate, and whitlockite. The proportions of each phase present in the samples are listed in Table 2.

The calcium phosphate series minerals are prone to have their signals obscured by the dominant HA due to the close proximity of their diffraction peaks as well as Raman and infrared spectral bands. ACP, generating weaker signals, is particularly susceptible to being overlooked and often treated as background substrate. Widely recognized as a precursor in animal hard tissue formation, such as zebrafish skeletal systems (Mahamid J et al., 2008) and murine enamel (Beniash E et al., 2009), ACP subsequently transforms into stable HA. In *in vitro* calcium phosphate synthesis experiments, ACP has been confirmed as the initial precipitated phase (Posner AS

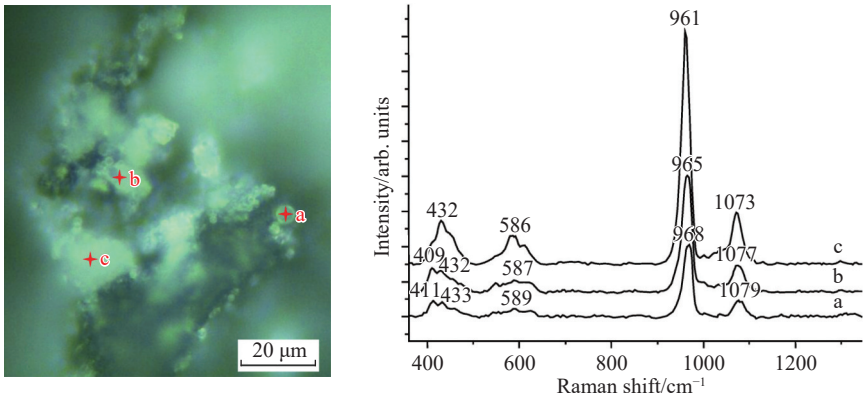

Fig. 15. Micro-Raman analysis of ductal carcinoma in situ sample YW-7. Left: Mineralization morphology under 50× objective lens. a–spherical mineralization; b–mixed area; c–blocky mineralization; Right: Corresponding Raman spectra of locations a, b, and c.

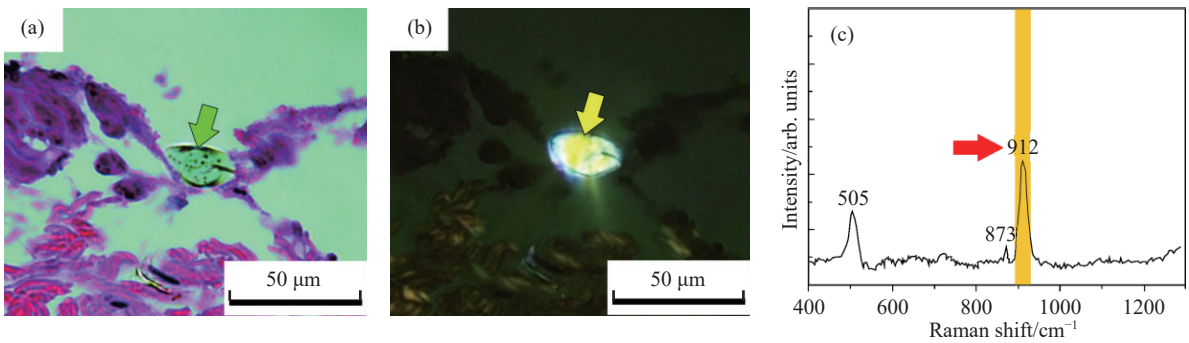

Fig. 16. Polarized light microscopy and Raman spectroscopic analysis of invasive breast carcinoma sample JR-8. a–histological image of type I mineralization under single-polarized light; b–extinction phenomenon of type I mineralization under cross-polarized light; c–Raman spectrum of type I mineralization.

Table 2. Occurrence and proportions of each phase in the samples.

	HA	ACP	Calcium oxalate	Whitlockite
Invasive carcinoma	25 / 25	25 / 25	1 / 25	0 / 25
Carcinoma in situ	15 / 15	15 / 15	1 / 15	2 / 15
Benign lesions	21 / 21	21 / 21	3 / 21	5 / 21

and Betts F, 1975), with ACP spherules gradually crystallizing into HA spheres during reaction progression. Dey A et al. (2010) utilized cryogenic transmission electron microscopy to image various mineralization stages, directly observing pre-nucleation clusters in solution aggregating on monolayer surfaces to form ACP spherules, followed by crystallization into HA. Our findings demonstrate the presence of ACP phase in breast lesion mineralization, with TEM observations revealing the coexistence of amorphous ACP and crystalline HA phases, indicating ongoing transformation from ACP to HA and suggesting ACP serves as HA precursor.

Whitlockite (chemical formula $Ca_{18}Mg_2[HPO_4]_2[PO_4]_{12}$), compared with HA, contains substantial magnesium in its structure, and its formation strongly correlates with magnesium concentration in the solution environment. Studies confirm that ACP precursors in solution can only transform into HA when Mg^{2+} concentration is low (LeGeros RZ, 2001), whereas elevated Mg^{2+} levels inhibit ACP-to-HA conversion while promoting whitlockite formation (Beniash E et al., 2009). Our research reveals that whitlockite exclusively occurs in benign lesions and carcinoma in situ samples, with higher prevalence in benign lesions (5/21 ≈23.8%) than in carcinoma in situ (2/15 ≈13.3%), while being absent in invasive carcinoma mineralization. This indicates distinct chemical environments among different breast lesion types leading to mineralization product variations. Furthermore, Baker R et al. (2010) noted that pathological mineralization properties in carcinoma in situ (carbonate content and organic/mineral ratio) consistently intermediate between benign lesions and invasive carcinoma, proposing potential progression from benign lesions through carcinoma in situ to invasive carcinoma. Additional studies demonstrate magnesium's bidirectional interaction with carcinogenesis: elevated Mg levels constitute a risk factor for postmenopausal breast cancer development (Leidi M et al., 2011), while Mg-deficient microenvironments impair DNA repair processes and cellular proliferation/apoptosis regulation (Wolf FI and Trapani V, 2012). Compared with healthy populations, breast cancer patients exhibit significantly reduced serum Mg levels (Abdelgawad IA et al., 2015). This suggests that during early-stage (benign) breast lesions, relatively high Mg concentrations in the local chemical environment permit ACP transformation into whitlockite. With disease progression and increasing malignancy, decreasing Mg^{2+} concentrations in the lesion microenvironment eliminate whitlockite from mineralization products.

In early studies, calcium oxalate was considered indicative of benign lesions or lobular carcinoma in situ with favorable prognosis (Busing C et al., 1981; Frappart F et al., 1986; Fandos-Morera A et al., 1988; Haka AS et al., 2002; Morgan MP et al., 2005), leading to insufficient attention towards calcium oxalate research in breast lesion mineralization. Concurrently, mineralization products experience partial loss during sample fixation, embedding, and sectioning processes, resulting in calcium oxalate detection in less than 5% of breast mineralization foci (Tse MT et al., 2008). Furthermore, the inherent difficulty in staining calcium oxalate crystals with conventional histological methods renders them particularly susceptible to being overlooked during routine histological observations.

Our findings reveal that calcium oxalate (either monohydrate or dihydrate) exists across all three lesion types. It not only occurs within HA-containing mineralization regions of benign lesions and carcinoma in situ (manifesting as Type I/II mixed mineralization), but also presents in invasive carcinoma samples. Previous research has demonstrated that calcium oxalate can promote malignant transformation of normal mammary epithelial cells by inducing proto-oncogene c-fos expression and breast cancer cell proliferation (Castellaro AM et al., 2015). If calcium oxalate is simplistically attributed to benign lesions and prognostically favorable lobular carcinoma in situ, while omitting subsequent biopsy examinations for calcium oxalate-positive cases, this practice may lead to underdiagnosis and/or misdiagnosis of substantial numbers of malignant breast lesions. These observations underscore that detailed classification of breast mineralization, whether through imaging, pathological analysis or mineralogical characterization, enhances diagnostic accuracy for breast lesions and provides valuable guidance for subsequent clinical interventions.

5. Conclusion

Breast cancer is one of the most common malignant tumors in women and a leading cause of cancer death among females. Its global incidence has been increasing annually in recent years. In 2022, new cases worldwide reached 2.3 million, accounting for 11.6% of all cancer diagnoses. Preventing and treating breast cancer has become an urgent global challenge and constitutes one of the significant issues addressed by the United Nations Sustainable Development Goals.

This study provides a detailed analysis of phase composition in breast lesion mineralization and investigates the presence and occurrence frequency of different mineral phases across three lesion types: Invasive carcinoma, carcinoma in situ and benign lesions. The results demonstrate that breast lesion mineralization predominantly comprises calcium phosphates, including ACP, whitlockite, and the predominant HA, occasionally accompanied by calcium oxalate. These phases can be differentiated through Fourier transform infrared spectroscopy combined with Raman spectroscopic analysis. Distinct variations exist in phase

distribution and prevalence among the three lesion types. HA is universally present and dominant across all sample categories. As a precursor phase, ACP, though widely formed during early mineralization stages, shows inconsistent preservation in tested specimens. Whitlockite exclusively occurs in carcinoma in situ and benign lesions, with higher prevalence in benign lesions (5/21 ≈23.8%) than in carcinoma in situ (2/15 ≈13.3%). Calcium oxalate is observed not only in HA-containing mineralization regions of benign lesions and carcinoma in situ, manifesting as Type I/II mixed mineralization, but also in invasive carcinoma mineralization.

Breast mineralizations play a critical role in mammary disease diagnosis, with its heterogeneous characteristics demonstrating potential diagnostic value for lesion classification. Research in mineralogy offers distinct perspectives and techniques for the screening and diagnosis of mineralization-related breast diseases. Multidisciplinary research is the key to solving problems and has broad prospects.

CRediT authorship contribution statement

Chang-qiu Wang, Xiao Cheng, Hong-rui Ding, Yan Li and An-huai Lu conceived of the presented idea. Xiao Cheng, Chang-qiu Wang and Hong-rui Ding carried out the experiment. All authors discussed the results and contributed to the final manuscript.

Declaration of competing interest

The authors declare no conflicts of interest.

Acknowledgments

This work was financially supported by the National Natural Science Foundation of China (41772033, 41272048). The authors gratefully acknowledge the technical assistance provided by Yan Zhang, Fang Mei, Kang Li, Chong-qing Yang, and Jing-yun Du during this research.

References

Abdelgawad IA, El-mously RH, Saber MM, Mansour OA, Shouman SA. 2015. Significance of serum levels of vitamin D and some related minerals in breast cancer patients. International Journal of Clinical and Experimental Pathology, 8(4), 4074–4082.

Baker R, Rogers KD, Shepherd N, Stone N. 2010. New relationships between breast microcalcifications and cancer. British Journal of Cancer, 103(7), 1034–1039. doi: 10.1038/sj.bjc.6605873.

Beniash E, Metzler RA, Lam RSK, Gilbert PUPA. 2009. Transient amorphous calcium phosphate in forming enamel. Journal of Structural Biology, 166(2), 133–143. doi: 10.1016/j.jsb.2009.02.001.

Busing C, Keppler U, Menges V. 1981. Differences in microcalcification in breast tumors. Virchows Archiv A-Pathological Anatomy and Histopathology, 393(3), 307–313. doi: 10.1007/BF00430830.

Castellaro A M, Tonda A, Cejas HH, Ferreyra H, Caputto BL, Pucci OA, Gil GA. 2015. Oxalate Induces Breast Cancer. BMC Cancer, 15, 761–773. doi: 10.1186/s12885-015-1747-2.

Chen SG. 1993. Identification of calcium oxalate crystals using polarized light microscopy. Primary Journal of Chinese Materia Medica, 7(2), 44–45 (in Chinese).

Choi S, Coonrod S, Estroff L, Fischbach, C. 2015. Chemical and physical properties of carbonated hydroxyapatite affect breast cancer cell behavior. Acta Biomaterialia, 24, 333–342. doi: 10.1016/j.actbio.2015.06.001.

Dey A, Bomans PHH, Müller FA, Will J, Frederik PM, de With G, Sommerdijk NAJM. 2010. The role of prenucleation clusters in surface-induced calcium phosphate crystallization. Nature Materials, 9(12), 1010–1014. doi: 10.1038/NMAT2900.

Dorozhkin SV. 2010. Nanosized and nanocrystalline calcium orthophosphates. Acta Biomaterialia. 6(3), 715–734. doi: 10.1016/j.actbio.2009.10.031

Fandos-Morera A, Prats-Esteve M, Tura-Soteras JM, Traveriacros, A. 1988. Breast Tumors: Composition of microcalcifications. Radiology, 169(2), 325–327. doi: 10.1148/radiology.169.2.2845471.

Fischmann A. 2008. Encyclopedia of Diagnostic Imaging. Berlin, Springer Berlin Heidelberg, 215–217.

Frappart L, Rcmy I, Lin HC, Bremond A, Raudrant D, Grousson B, Vauzelle JL. 1986. Different types of microcalcifications observed in breast pathology-Correlations with histopathological diagnosis and radiological examination of operative specimens. Virchows Archiv A-Pathological Anatomy and histopathology, 410(3), 179–187.

Frondel C 1943. Mineralogy of the calcium phosphates in insular phosphate rock. American Mineralogist, 28(4), 215–232.

Frouge C, Guinebretiere J M, Juras J, Fertil B, Benali H, Contesso G, DiPaola R, Blery M. 1996. Polyhedral microcalcifications on mammograms: Prevalence and morphometric analysis. American Journal of Roentgenology, 167(3), 621–624. doi: 10.2214/ajr.167.3.8751664.

Ghita A, Matousek P, Stone N. 2018. Characterisation of a novel transmission Raman spectroscopy platform for non-invasive detection of breast micro-calcifications. In: MahadevanJansen, A. and Petrich, W. (eds), Biomedical Vibrational Spectroscopy 2018: Advances in Research and Industry, 140490. doi:10.1117/12.2297632

Haka AS, Shafer-Peltier KE, Fitzmaurice M, Crowe J, Dasari RR, Feld MS. 2002. Identifying microcalcifications in benign and malignant breast lesions by probing differences in their chemical composition using Raman spectroscopy. Cancer Research, 62(18), 5375–5380.

Hanawalt JD, Rinn HW, Frevel LK. 1938. Chemical analysis by X-ray diffraction- Classification and use of X-ray diffraction patterns. Industrial and Engineering Chemistry-Analytical Edition, 10, 457–512. doi: 10.1021/ac50125a001.

Kerssens M. 2012. Study of Calcification Formation and Disease Diagnostics Utilising Advanced Vibrational Spectroscopy. Bedford, Cranfield University, Ph. D thesis, 116–160.

Leidi M, Wolf FI, Maier JAM. 2011. Magnesium in the Central Nervous System. Adelaide, University of Adelaide Press, 217–228.

LeGeros RZ. 2001. Formation and transformation of calcium phosphates: Relevance to vascular calcification. Zeitschrift Für Kardiologie, 90(3), 116–124.

Ling H, Liu ZB, Xu LH, Xu XL, Liu GY, Shao ZM. 2013. Malignant calcification is an important unfavorable prognostic factor in primary invasive breast cancer. Asia-Pacific Journal of Clinical Oncology, 9(2), 139–145. doi: 10.1111/j.1743-7563.2012.01572.x.

Mahamid J, Sharir A, Addadi L, Weiner S. 2008. Amorphous calcium phosphate is a major component of the forming fin bones of zebrafish: Indications for an amorphous precursor phase. Proceedings of the National Academy of Sciences of the United States of America, 105(35), 12748–12753. doi: 10.1073/pnas.0803354105.

Martin HM, Bateman AC, Theaker JM. 1999. Calcium oxalate (Weddellite) crystals within ductal carcinoma in situ. Journal of Clinical Pathology, 52(12), 932–932. doi: 10.1136/jcp.52.12.932.

Meng FL, Li Y, Li Y, Wang CQ, Lu AH, Meng F. 2015.

Characterization of human breast cancer calcification using synchrotron radiation. Acta Petrologica et Mineralogica, 34(6), 957–962 (in Chinese with English abstract).

Morgan MP, Cooke MM, McCarthy GM. 2005. Microcalcifications associated with breast cancer: An epiphenomenon or biologically significant feature of selected tumors?. Journal of Mammary Gland Biology and Neoplasia. 10(2), 181–187. doi: 10.1007/s10911-005-5400-6

Obenauer S, Hermann KP, Grabbe E. 2005. Applications and literature review of the BI-RADS classification. European Radiology, 15(5), 1027–1036. doi: 10.1007/s00330-004-2593-9.

O'Grady S, Morgan MP. 2018. Microcalcifications in breast cancer: From pathophysiology to diagnosis and prognosis. Biochimica et Biophysica Acta - Reviews on Cancer, 1869(2), 310–320. doi: 10.1016/j.bbcan.2018.04.006.

Posner AS, Betts F. 1975. Synthetic amorphous calcium phosphate and its relation to bone mineral structure. Accounts of Chemical Research, 8(8), 273–281. doi: 10.1021/ar50092a003.

Rey C, Lian J, Grynpas M, Shapiro F, Zylberberg L, Glimcher MJ. 1989. Non-apatitic environments in bone mineral: FT-IR detection, biological properties and changes in several disease states. Connective Tissue Research, 21(1-4), 597–603. doi: 10.3109/03008208909050016.

Saha A, Barman I, Dingari NC, McGee S, Volynskaya Z, Galindo LH, Liu W, Plecha D, Klein N, Dasari RR, Fitzmaurice M. 2011. Raman spectroscopy: A real-time tool for identifying microcalcifications during stereotactic breast core needle biopsies. Biomedical Optics Express, 2(10), 2792–2803.

Scimeca M, Giannini E, Antonacci C, Pistolese CA, Spagnoli LG, Bonanno E. 2014. Microcalcifications in breast cancer: an active phenomenon mediated by epithelial cells with mesenchymal characteristics. BMC Cancer, 14(1), 286. doi: 10.1186/1471-2407-14-286.

Scott R, Kendall C, Stone N, Rogers K. 2017. Elemental vs. phase composition of breast calcifications. Scientific Reports, 7, 136. doi: 10.1038/s41598-017-00183-y.

Siegel RL, Miller KD, Jemal A. 2016. Cancer statistics, 2016. CA - A Cancer Journal for Clinicians, 66(1), 7–30. doi: 10.3322/caac.21332.

Stone N, Matousek P. 2008. Advanced transmission Raman spectroscopy: a promising tool for breast disease diagnosis. Cancer Research, 68(11), 4424–4430. doi: 10.1158/0008-5472.CAN-07-6557.

Tse MT, Tan PH, Cheung HS, Chu WCW, Lam WWM. 2008. Intermediate to highly suspicious calcification in breast lesions: a radio-pathologic correlation. Breast Cancer Research and Treatment, 110(1), 1–7. doi: 10.1007/s10549-007-9695-4.

Wang CQ, Zhao WW, Lu AH, Xiong CE, Meng F, Liu JY. 2011. Characteristics of Mineralized Focuses in Several Breast Diseases. Geological Journal of China Universities, 17(1), 29–38 (in Chinese with English abstract). doi: 10.16108/j.issn1006-7493.2011.01.001.

Wang ZT, Hauser N, Singer G, Trippel M, Kubik-Huch RA, Schneider CW, Stampanoni M. 2014. Non-invasive classification of microcalcifications with phase-contrast X-ray mammography. Nature Communications, 5, 3797. doi: 10.1038/ncomms4797.

Winston JS, Yeh IT, Evers K, Friedman AK. 1992. Calcium oxalate is associated with benign breast tissue: Can we avoid biopsy?. American Journal of Clinical Pathology, 100(5), 488–492. doi: 10.1093/ajcp/100.5.488.

Wolf FI, Trapani V. 2012. Magnesium and its transporters in cancer: a novel paradigm in tumour development. Clinical Science, 123(7-8), 417–427. doi: 10.1042/CS20120086.

Xu CQ, Karan K, Yao XM, Wang Y. 2009. Molecular structural analysis of noncarious cervical sclerotic dentin using Raman spectroscopy. Journal of Raman Spectroscopy, 40(12), 1780–1785. doi: 10.1002/jrs.2320.

You AF, Bergholt MS, St-Pierre JP, Kit-Anan W, Pence IJ, Chester AH, Yacoub MH, Bertazzo S, Stevens MM. 2017. Raman spectroscopy imaging reveals interplay between atherosclerosis and medial calcification in the human aorta. Science Advances, 3(12), e1701156. doi: 10.1126/sciadv.1701156.